6. Controlling nanoparticle behaviour by use of electrical effects

A control of gas-phase nanoparticle synthesis is possible on the basis of the movement of charged particles in an electric field. This allows size fractionation, direct particle size measurement, deposition of nanoparticles onto suitable substrates and controlled mixing.

This requires nanoparticles which are charged. Therefore, a charger especially suited for nanoparticles is needed. In the newly developed twin Hewitt charger two corona discharge zones are connected by a charging zone where the nanoparticle aerosol flows. Ions move into the charging zone alternating from each corona discharging zone by means of a square-wave voltage. The operation parameters of the device are experimentally characterized and described in Chapter 6.1 with the goal to optimize the charging efficiency in N_2 carrier gas. The contents of this subchapter has been published (Kruis and Fissan, 2001).

Most nanoparticle formation paths in the gas phase involve particle growth induced by particle collision due to the Brownian motion. This leads to a minimum geometric standard deviation of 1.4 (see Fig. 4.2.5), which is further increased by turbulence and variations in residence time. Narrowing the size distribution is possible by use of a DMA at the cost of decreased particle number concentration. The standard DMA design is, however, not suitable for use at sub-atmospheric pressures. Lower pressures are desirable for the synthesis because it will lead to a smaller mean particle size and to a reduction of gas-phase impurities. Therefore, a new DMA has been designed to operate at lower pressures. Theoretical and practical considerations for the design will be shown in Chapter 6.2.

The application of the so-called electrical mobility analysis allows the direct measurement of particle size distributions. For this goal, a DMA is connected to a particle counter such as a condensation nucleus counter or an electrometer. An inversion technique combined with the transfer function of the DMA and the charging efficiency of the charging device allows to calculate the particle size distribution. This technique will also benefit from an increased charging efficiency, as this increases the sensitivity in the nanoparticle size range. Furthermore, a DMA capable for operating at lower processes enables size measurements in low pressure reactors, which are used in industry for TiO_2 , SiO_2 and soot particle synthesis.

The characterization of the electrical properties of thin nanoparticle films was hampered by problems of contamination of the samples by air as the sample was transported from the reactor to measurement set-up. A nanoparticle film formation

device, basing on electrostatic deposition, which enables measurement under clean conditions will be described in Chapter 6.3.

6.1 Nanoparticle charging using a twin Hewitt charger

One important way of obtaining control over their movement is manipulation of charged nanoparticles in an electric field. This can be used for the generation of monodisperse particles by means of a Differential Mobility Analyzer at atmospheric conditions, as will be shown in chapter 7, or by means of a time of flight Mass Spectrometer in a high vacuum (Ehbrecht *et al.,* 1997). It is also essential when using electrostatic deposition.

Nanoparticle charging at standard temperature and pressure is possible by means of unipolar or bipolar diffusion charging. Unipolar ions are commonly generated by means of a corona discharge whereas bipolar ions are generated by means of radioactive sources, either α or β sources such as ^{85}Kr or ^{241}Am. Bipolar charging leads to a charge equilibrium which has however low charging efficiencies, e.g. 3.3 % for positively charged 10 nm particles and 5.7 % for negatively charged particles (Wiedensohler, 1988). Unipolar diffusion charging has advantages over bipolar diffusion charging as it does not reach an equilibrium charge distribution, therefore potentially enabling the attainment of a higher charging efficiency. However, considerable difficulties arise because of large losses due to electrostatic effects as soon as the particles are charged.

In unipolar chargers using a corona discharge the particle-laden carrier gas is passed along a wire mesh around a corona wire, either over some part of it (Hewitt, 1957) or over the whole circumference (Büscher *et al* , 1994). Already in the first unipolar charging device described in 1957 by Hewitt a square wave voltage was applied between the wire mesh and the other side of the charging zone in order to reduce particle losses of charged particles in the electric field. A steady electric field would lead to large losses of charged particles. However, during only 50 % of the time ions fill the charging zone, during the other period they are expelled by the reversed field. In another diffusion charger (Wiedensohler *et al.,* 1994) in which ions are produced by a radioactive source, the charging zone is filled from two sides with ions, in each square-wave period from a different side. The most recent developed nanoparticle charger (Chen and Pui, 1999) uses a radioactive source, a charging zone with a longitudinal electric field and a large sheath gas flow in order to minimize losses to the walls.

Here, the advantages of the different chargers are combined into one new charger, which might be called a twin Hewitt charger. In this device, two corona discharge zones are connected by a charging zone. The particle-carrying gas flow is

parallel to the corona wires and the wire mesh. Ions move into the charging zone alternating from each corona discharging zone by means of a square-wave voltage between the two wire meshes.

6.1.1 Experimental setup

6.1.1.1 The twin Hewitt charger

Fig. 6.1.1 shows the schematic diagram of the newly developed twin Hewitt charger. The particle-laden gas is introduced via a short inlet section into a square charging zone with a width of 16 mm and a height of 10 mm. The charging zone is separated from the two ion production zones by means of metal wire meshes, and the bottom and top are composed of isolating material. The wire screens are connected to two square-wave generators with opposite phase and a maximal voltage difference ΔV of 600 V. The use of the square wave with a frequency f allows the use of a relatively large potential between both grids which results in a high ion concentration in the charging zone. The use of a non-alternating field would lead to a continuous movement of the charged particles toward the wire mesh.

Positive ions are produced by corona discharge of a 25 µm thick Au wire placed in the center of in a metal cylinder, which has at one side a slit of a length 15 cm and a height 1 cm. This slit is placed towards the charging zone and is covered with the wire mesh. The careful handling of the thin Au wire is critical for obtaining a long life time of the wire. The wire attached by glue to a needle is inserted through the openings at the end of the cylinder, and immobilized by means of a isolation strip and a drop of glue. Its' electrical contact is made by means of a drop of silver paste.

The length of the charging zone L with a maximum length of 15 cm can be adjusted by covering part of the wire meshes with thin Al sheets. The exposed wire meshes are always as close to the exit as possible.

Initial measurements using a constant high voltage connected to the coronas showed problems with stability and reproducibility. This problem was solved by using two different high voltage sources which were so regulated that a constant current in the range 10 to 100 µA was obtained. The largest part of this current will flow via the cylinder and the square-wave generators, which are electrically connected, towards ground potential. This did not affect the functioning of the square-wave generators, which was checked by means of an oscilloscope.

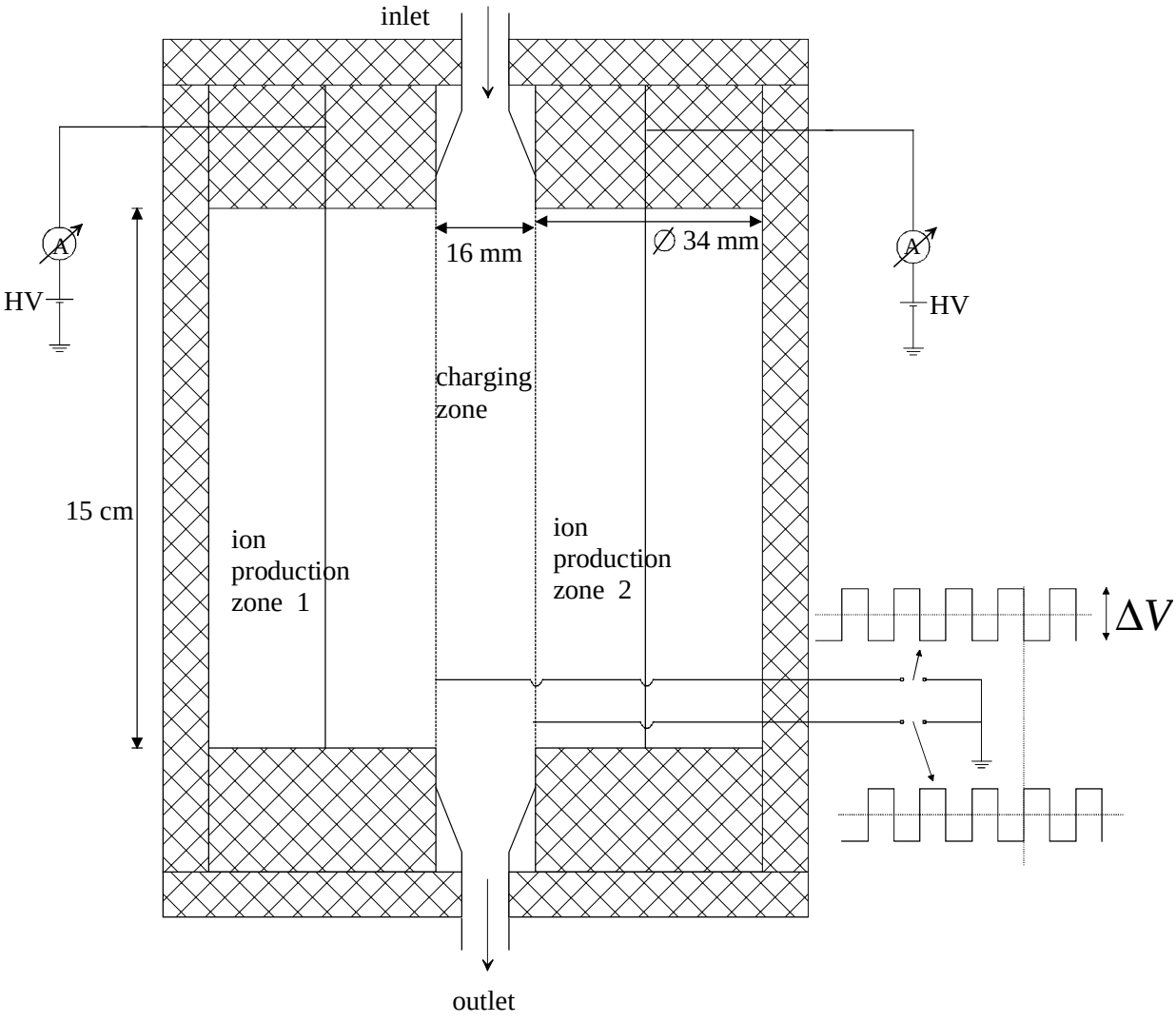

Fig. 6.1.1. Schematic diagram of the twin Hewitt charger. Ions are produced in two cylindrical sections with a central Au wire with a diameter of 25 µm and move through a slit covered with wire mesh into the charging zone. A square wave electric potential is established between both wire meshes.

6.1.1.2 Setup for measuring charging efficiencies

Fig. 6.1.2 shows the schematic diagram of the experimental setup used in measuring the charging efficiency. It consists of four parts: a generator of monodisperse particles, a device used for discharging the particles, the twin Hewitt charger and the measurement section for distinguishing charged and uncharged particles.

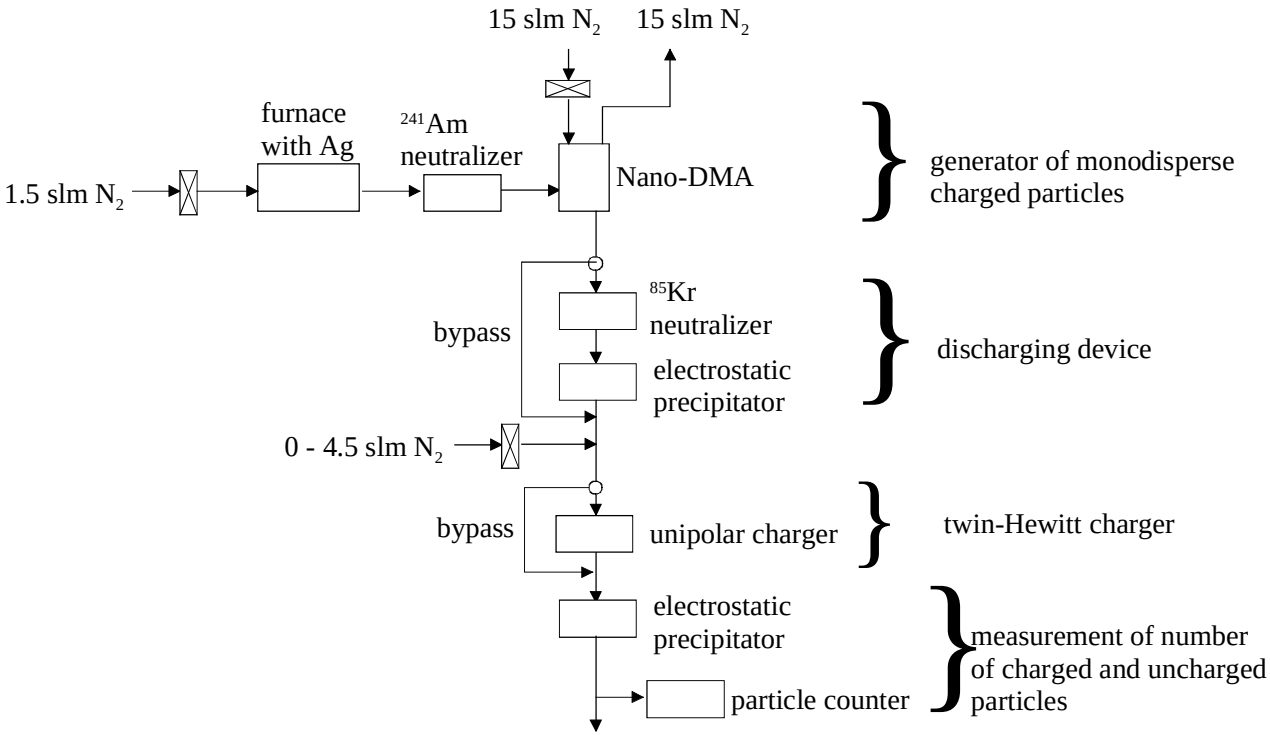

Fig. 6.1.2. Experimental setup for measuring the charging efficiency of a unipolar charger. A nanoparticle aerosol is generated by means of evaporation-condensation, size-classified by means of a Differential Mobility Analyzer (DMA) and subsequently discharged. After being charged in the twin-Hewitt charger, the particles pass an electrostatic precipitator after which the number concentration is monitored by means of a particle counter.

The aerosol generator consists of a furnace in which Ag is evaporated, followed by condensation in the cooler parts of the tube. The nanoparticles thus formed are partially charged using a radioactive source and are then classified according to their electric mobility by means of a Nano-DMA (Chen *et al.*, 1998) to obtain a well-defined test aerosol. When using a carrier gas flow of 1.5 slm (standard liters per minute) and an additional flow of 15 slm through the Nano-DMA (TSI, Minneapolis, USA), a theoretical GSD of 1.1 is attained for the classified aerosol and can therefore be called monodisperse. The experiments are performed with N_2 as carrier gas at standard conditions (1 bar, 293 K). The flow through the tube furnace and DMA was fixed at 1.5 slm. The use of dilution gas allowed the gas flow rate through the charger to be adjusted between 1.5 slm and 6 slm.

The particles leaving the DMA are charged which is undesirable for the charging measurements. Therefore, they are led through a radioactive neutralizer which partially neutralizes the particles. The fraction which is still charged is removed in an electrostatic precipitator, which consists of a annular tube with a high electric

field intensity (2 kV/cm). The discharging section can also be bypassed in order to produce monodisperse charged particles for the measurement of electric losses in the charger.
After being charged in the twin-Hewitt charger, the particles pass a second electrostatic precipitator before being counted in a particle counter (UCPC 3025, TSI, Minneapolis, USA) which has a detection threshold of about 3 nm. The number concentration of charged particles n_+ is determined by taking the difference between particles counted without an electric field (giving $n_+ + n_0$) applied in the electrostatic precipitator and particles counted with an electric field applied field (giving the number concentration of uncharged particles n_0) applied. The extrinsic charging efficiency can be calculated by the following equation:

$$E_e = \frac{n_+}{n_{in}} \tag{6.1.1}$$

where n_{in} is the number concentration of particle entering the charger. The charging thus defined is called extrinsic because the charging efficiency is actually higher, but charged particles are lost more easily than uncharged particles. In the remainder of this article, when referring to charging efficiency the extrinsic charging efficiency is meant. The intrinsic charging efficiency E_i is defined as the fraction of particles which are charged inside the charger, but which also can be lost there.

6.1.2 Ion concentration in the charging zone

In this section, the ion concentration in the charging section is estimated. The charging zone is in between $x = 0$ and $x = a$, a is the width of the charging channel. We calculate the electrical field $E(x)$ and the ion concentration $n(x)$ for the case of constant grid voltage. On the basis of Maxwell's theory, the electrical field between the two grids can described by:

$$\text{div}\,\vec{E} = \frac{\rho(x)}{\varepsilon_0} \tag{6.1.2}$$

where $\rho(x)$ is the space charge density and ε_0 the dielectric constant of vacuum. As the upper and lower end of the charging channel is an isolator, we assume that the field lines do only have a component in x-direction:

$$\frac{dE(x)}{dx} = \frac{\rho(x)}{\varepsilon_0} \tag{6.1.3}$$

The ion current density $\vec{j}$ is given by:

$$\vec{j} = \rho \vec{v} \tag{6.1.4}$$

The ion velocity v_{ion} is determined by:

$$v_{ion}(x) = Z_{ion}\ E(x) \tag{6.1.5}$$

where Z_{ion} is the electric mobility of the ions. The current density can be expressed on the basis of the ion current I through the grid, which has an effective area of wL, as:

$$\rho(x)\ Z_{ion}\ E(x) = \frac{I}{wL} \tag{6.1.6}$$

The space charge defines the ion concentration:

$$\rho = n_{ion} e \tag{6.1.7}$$

so that the space charge can be eliminated, leading to a differential equation for $E(x)$:

$$E(x) = \sqrt{\frac{2Ix}{wLZ_{ion}\varepsilon_0} + c} \tag{6.1.8}$$

In order to determine I and n_{ion} from experiments, we have to solve:

$$\int_0^a E(x)dx = \Delta V \tag{6.1.9}$$

leading to

$$\frac{wLZ_{ion}\varepsilon_0}{3I}\left\{\left(\frac{2Ia}{wLZ_{ion}\varepsilon_0} + c\right)^{3/2} - c^{3/2}\right\} = \Delta V \tag{6.1.10}$$

For each pair $(\Delta V, I)$ we can determine c by solving this equation iteratively and determine the ion concentration in the charging zone:

The ion current per unit area of wire mesh I / wL, measured with constant electric field applied over the charging zone, showed little dependence on the length of the charging zone, as expected. Using the model the ion concentration can be calculated based on the experimental values of the ion current. The product of ion concentration and time $n_{ion}t$, an important parameter in the charging process, is shown in Fig. 6.1.3. The ion concentration varies over the width of the charging zone, therefore the ion concentration in the middle of the charging zone is taken. Increasing L or decreasing the flow rate for ϕ yield a higher value of $n_{ion}t$. The nonlinear increase of $n_{ion}t$ indicates that the ion concentration is not constant at various L. A possible explanation is that the electric field will extend beyond the charging zone into the aerosol in- and outlet, leading to a higher effective length. This boundary effect is obviously less important at higher L.

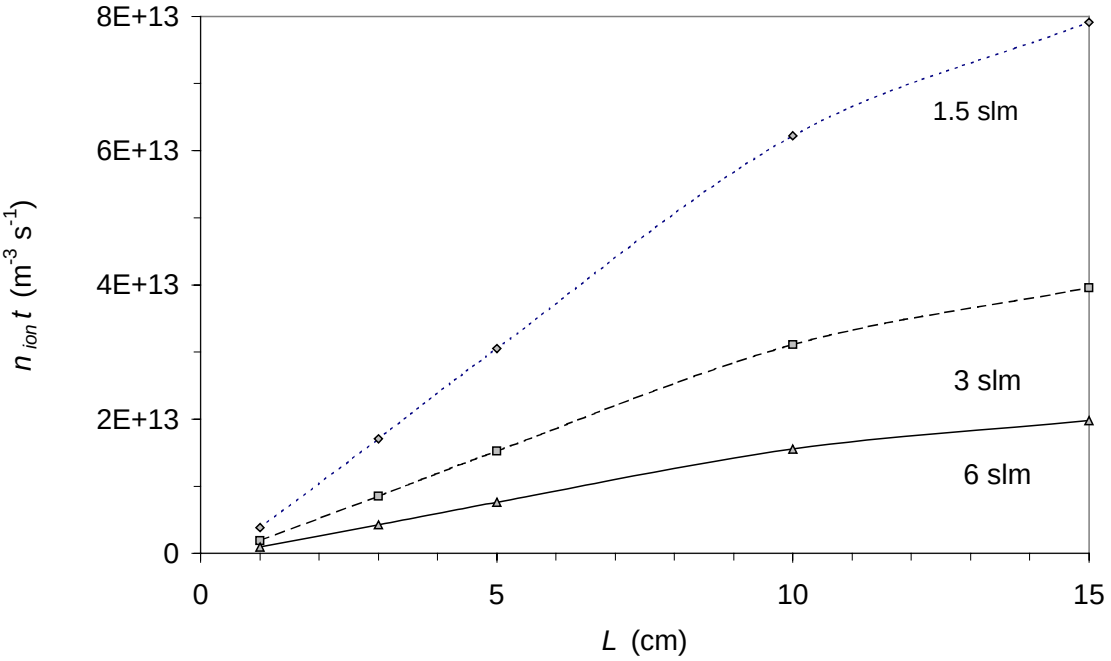

Fig. 6.1.3. The product of ion concentration and time $n_{ion}t$ *as function of the length of the charging zone L for different flow rates as indicated in the figure.* n_{ion} *is calculated at* $x = \frac{1}{2}a$.

6.1.3 Charging efficiency

6.1.3.1 Effects of frequency and electrical potential

The charging efficiency was measured as function of the square wave frequency and the voltage difference applied between the two meshes in order to find the best operating conditions. The extrinsic charging efficiency as function of the frequency is shown in Fig. 6.1.4 for different particle sizes. At frequencies above 100 Hz, the extrinsic charging efficiency decreases but is almost constant below 100 Hz. Frequencies below 10 Hz result in undesirable fluctuations of the high voltage of the corona wires, as the voltage supply is used in the constant current mode. In the remainder of the experiments a frequency of 50 Hz was used.

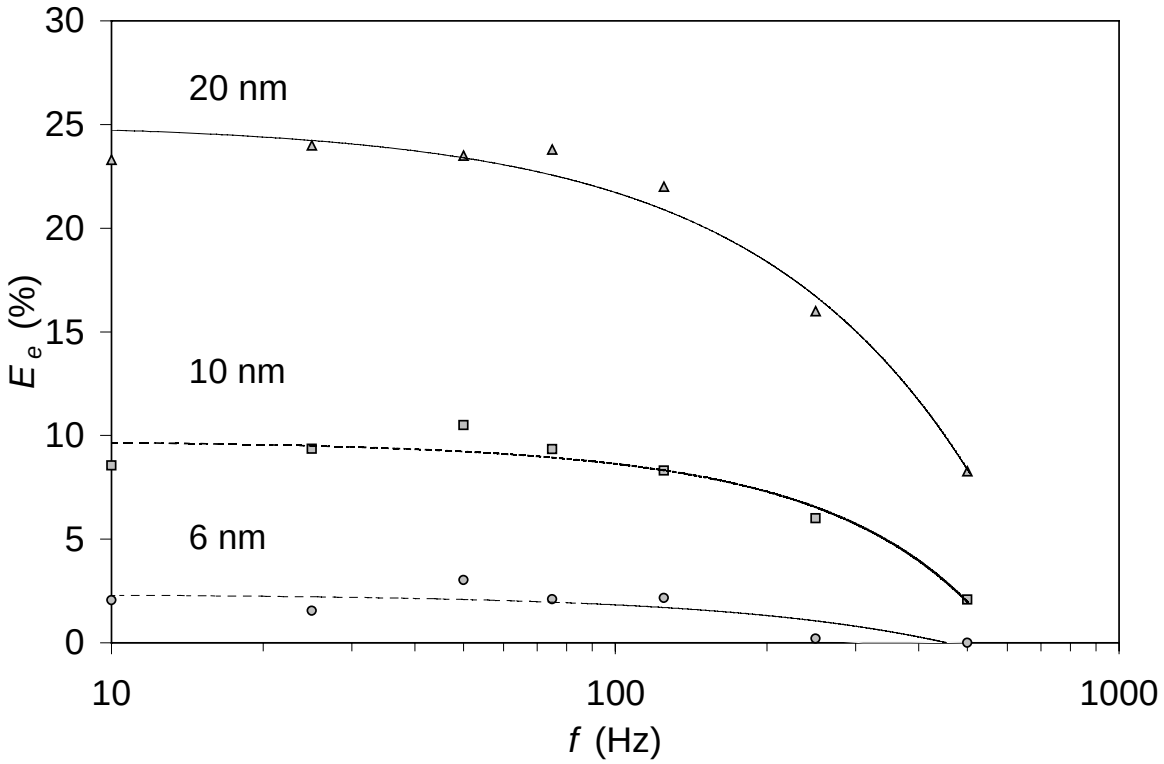

Fig. 6.1.4. Extrinsic charging efficiency as function of the frequency of the square wave generator for different particle sizes. Further conditions were I_c = 50 μA, ΔV = 400 V, ϕ = 1.5 slm , L = 15 cm.

Fig. 6.1.5 shows the extrinsic charging efficiency as function of the voltage difference ΔV using the whole length of the charging zone, L = 15 cm. After an initial increase, the charging efficiency E_e is not affected by the value of ΔV when ΔV >300V. Using a very short charging zone, L = 1 cm, E_e steadily increases with ΔV . The increase seems to level off around 600 V. Higher voltage differences could not be applied as the current through the square wave generators became too high. Therefore, ΔV = 600 V seemed to be optimal for obtaining a high charging efficiency for all lengths of charging zones.

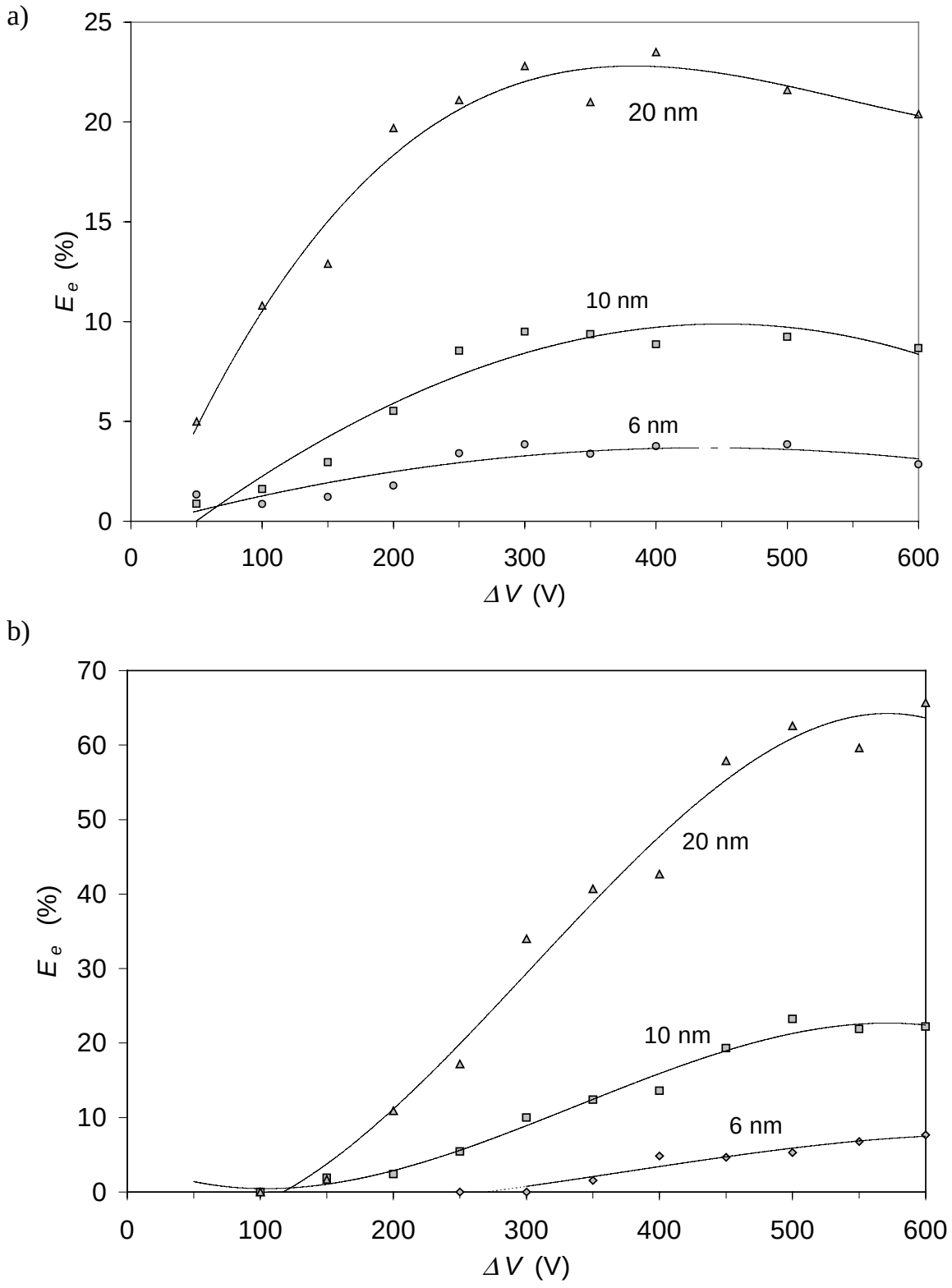

Fig. 6.1.5. Extrinsic charging efficiency as function of the voltage difference ΔV between the wire meshes for (a) L = 15 cm and (b) L = 1 cm. Further conditions were I_c = 50 µA, f = 50 Hz, ϕ = 1.5 slm.

6.1.3.2 Effects of length of charging zone and residence time

After obtaining a lower charging efficiency than we expected with L = 15 cm, we decided to perform a systematic study into the effect of the length of the charging zone. The method described earlier for obtaining a variable length is not ideal because the shorter charging zones have a relatively long entrance zone which causes some diffusion losses. This will be discussed later on. Building differently sized chargers is however unpractical and uneconomical. The lowest flow rate through the charger ϕ was 1.5 slm, a common flow rate when operating DMAs. For material synthesis applications, higher flow rates are desirable so this flow rate was increased to 3 and 6 slm in order to investigate the effect of having a shorter residence time in the charger. The residence times in the charging zone with L = 15 cm are τ = 0.96, 0.46 and 0.23 s for 1.5, 3 and 6 slm, resp.

Fig. 6.1.6 shows the effect of varying L and ϕ for particles with diameter 6 nm (Fig. 6.1.6a), 10 nm (Fig 6.1.6b) and 20 nm (Fig 6.1.6c). For each particle size and ϕ there exists a length where E_e is maximal. This length is L = 3-5 cm for ϕ = 1.5 slm and around L = 10 cm for ϕ = 6 slm, independent of particle size. For larger flow rates clearly a longer charging zone is needed. Furthermore, when the particles become smaller it seems to become increasingly difficult at higher flow rates to reach the same charging efficiencies as with ϕ = 1.5 slm by changing L.

a)

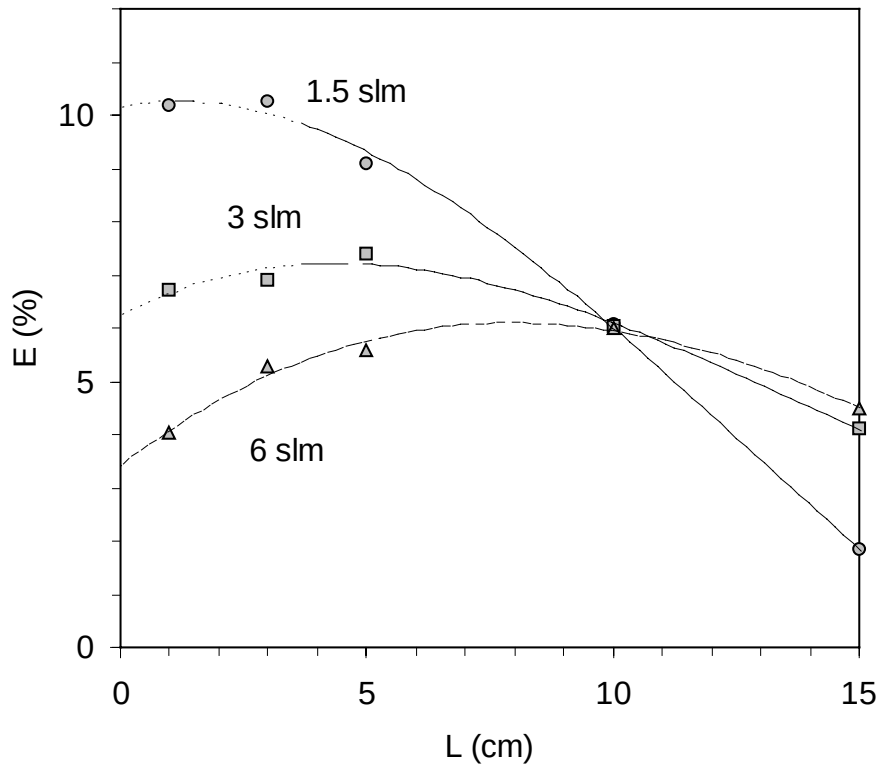

b)

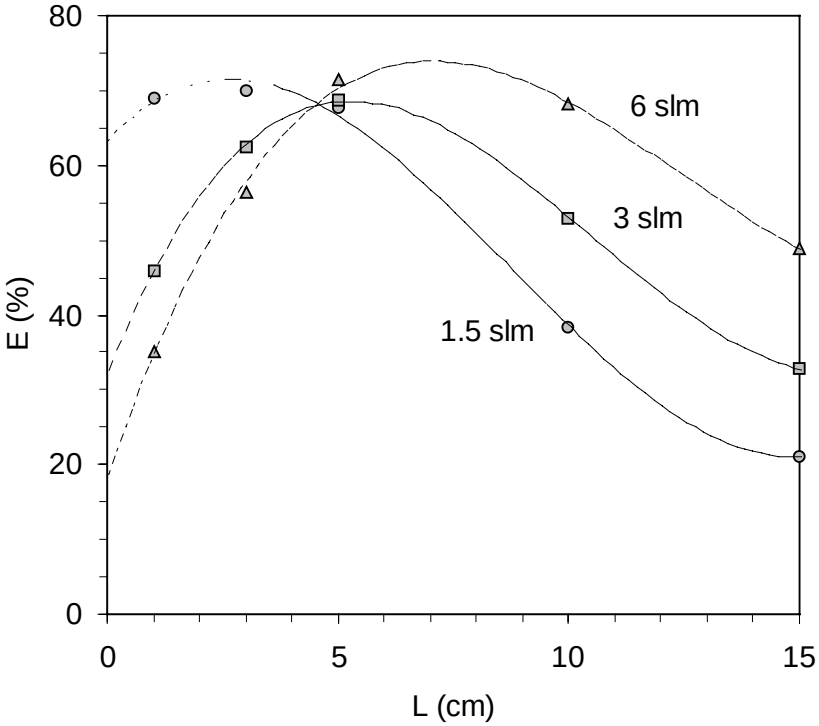

c)

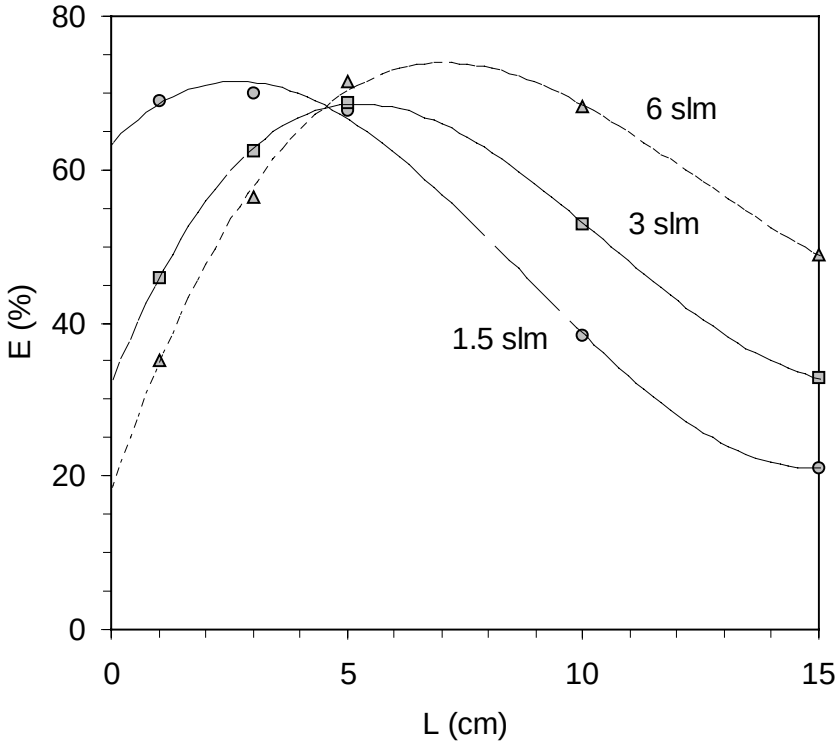

Fig. 6.1.6. Extrinsic charging efficiency as function of the length of the charging zone, for particles with a diameter of (a) 6 nm, (b) 10 nm and (c) 20 nm. The gas flow rates ϕ were varied as indicated in the figures. Operating conditions were I_c = 50 µA, ΔV = 600 V and f= 50 Hz.

Fig. 6.1.7 shows the charging efficiency E_e as function of the particle size up to 50 nm, for ϕ =1.5 slm (Fig 6.1.7a) and 6 slm (Fig 6.1.7b). Decreasing the particle size also decreases E_e, below 6 nm the efficiency becomes too low for accurate measurement and for practical application.

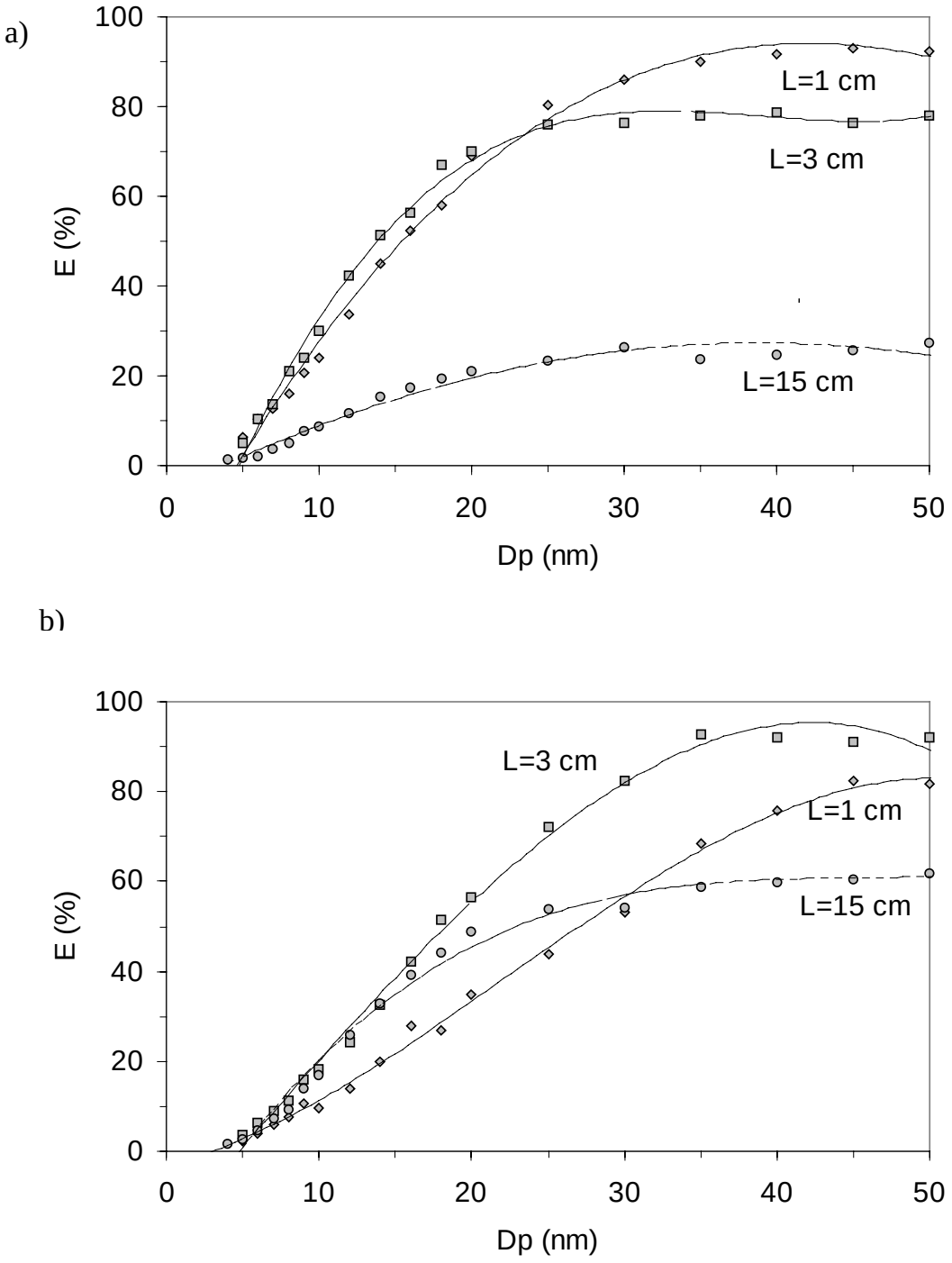

Fig. 6.1.7. Extrinsic charging efficiency as function of particle diameter for a flow rate of (a) 1.5 slm and (b) 6 slm. Curves for different lengths of the charging zone L are shown. Operating conditions as in Fig. 6.1.5.

6.1.4 Particle losses in the charging zone

A key in understanding the performance of a nanoparticle charger lies in understanding by what mechanisms the particles are lost. There are several mechanisms which might be responsible for the particle losses:

(i) The Brownian diffusion losses affects both charged and uncharged particles.

(ii) The oscillation of charged particles due to the alternating electrical field will lead to particles moving toward the wire mesh, so that particles relatively close to the wire mesh will be lost there.

(iii) The space charge due to the unipolar ions in the charging zone will drive charged particles toward the walls, which are the wire meshes and the upper and lower isolated parts of the channel. This is difficult to describe by a model, because the system is two-dimensional and periodically changing.

(iv) Electrostatic effects which will be especially important for the aerosol in the vicinity of the isolating material at the top and bottom of the charging channel. The material can become charged due to static electricity or deposition of charged particles.

Especially the last two effect are very difficult to model, so a series of experiments were done to investigate the importance of particle losses. The experiments were performed with charged particles, as diffusion losses of uncharged particles were found to be small in magnitude compared to the losses of charged particles. The results are shown in Fig. 6.1.8. Most experiments were performed with the longest charging section (L=15 cm), because this is the system with the largest losses.

First consider the case (a) with ϕ=6 slm and ΔV=0 V, so without applied field. The fraction of charged particles lost increases with decreasing particle sizes, because smaller particles have a higher electrical mobility, so that they are more ‘sensitive’ to electrical fields and electrostatic effects. Applying now the square wave potential over the charging channel, case (b), no significant change in the particle loss is observed. This means that effect (ii), losses due to the oscillation of the particles, is probably not very important and that the effects (iii) and (iv) are dominant. When the gas flow rate ϕ is decreased to 1.5 slm, case (c), the losses are seen to increase, except for particles below some 10 nm. It is probable that a kind of layer exists next to the walls and wire meshes of the charging channel, where particles have a high probability of being lost by mechanism (ii) or (iv). The width of this layer will be larger for smaller particles. A longer residence time increases the probability that charged particles enter this layer by Brownian diffusion or space charge effects, and furthermore the longer the particles remain in this layer next to the wall, the higher the probability they will get lost. This is clearly illustrated by comparison of case (c) for L=15 cm and (d) for L=3 cm. The losses for L=3 cm are a factor of 5-8 smaller than for L=15 at this low gas flow rate.

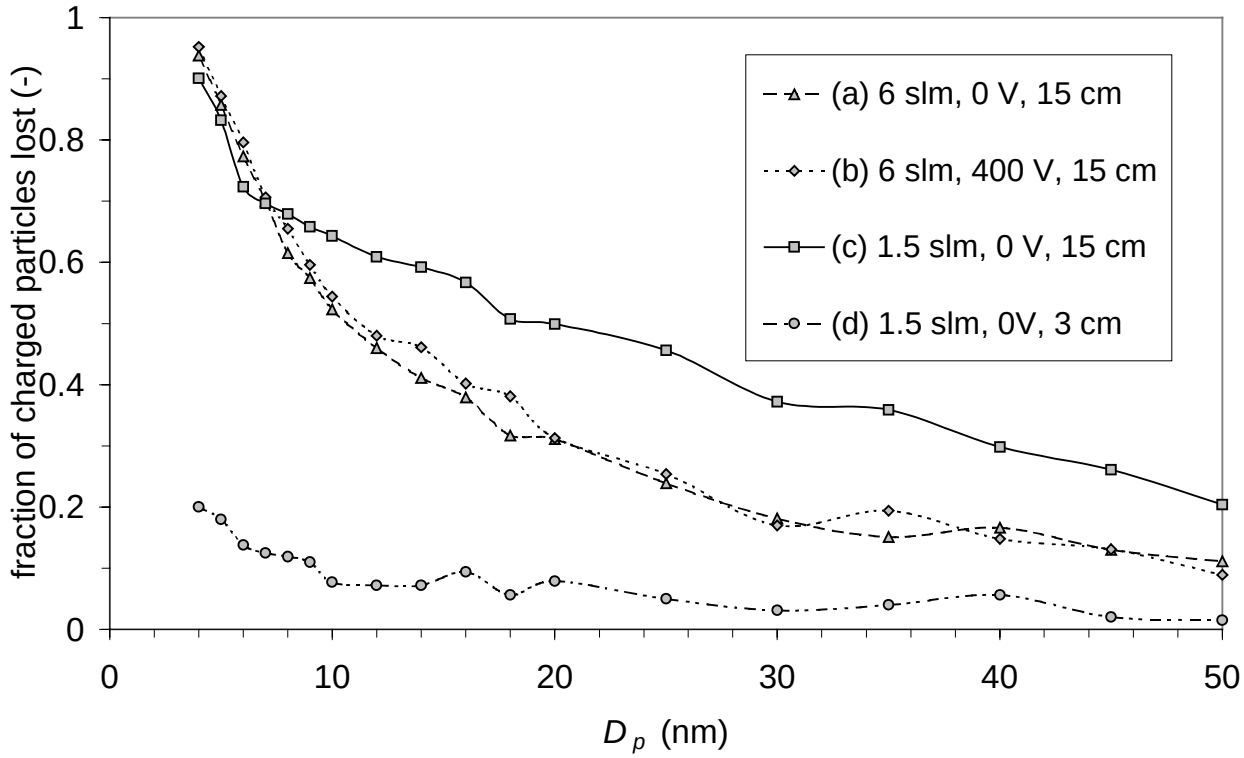

Fig. 6.1.8. Fraction of charged particles lost as function of particle diameter. The insert shows the values of the gas flow rate ϕ, voltage difference ΔV and length of the charging zone L, respectively.

In an attempt to reduce the electrostatic losses, the isolating material (DELRIN^{TM}) which composes the top and bottom of the charging channel was replaced by an antistatic material which allows charges to dissipate due to a moderate resistivity in the range of GΩ cm. The losses of charged particles were clearly reduced but the charging efficiency dropped dramatically. The electrical field lines will probably not any more be connecting the two wire meshes, but will lead from the wire meshes toward the bottom and top of the charging material. This leads to a loss of ions and a decrease in the $n_{ion}t$-product. The use of isolating material might be advantageous due to the fact that the material becomes slightly charged due to deposition of ions and charged particles, which can repel charged particles from the walls. Therefore, care was taken to run the charger in the charging mode before making measurements.

6.1.5 Discussion

The decreasing charging efficiency with increasing frequency of the square wave (Fig. 6.1.4) is due to the finite time it takes to fill the charging channel with ions in a new period. At a too high frequency, the ion concentration in the channel is not yet at

its' maximum. The mean ion concentration will therefore drop above a certain frequency, thereby lowering the charging efficiency. Increasing the voltage difference ΔV over the charging channel (Fig. 6.1.5) also increases the ion concentration. Above ΔV =500 V the increase in charging efficiency starts to level off, probably because the particle loss mechanisms (ii) and (iii) which are dependent on the applied field become more dominant.

The maximum in the charging efficiency as function of the length L of the charging channel (Fig. 6.1.6) is more complicated to understand. From the measurements of the losses of charged particles (Fig. 6.1.8), it is clear that a smaller value of L leads to a significant decrease in charged particle losses. At the same time, however, the $n_{ion}t$ -product which influences directly the intrinsic charging efficiency drops with lower L. From Fig. 6.1.3 it can be seen that the decrease in the $n_{ion}t$ -product is more pronounced at lower values of L, probably due to non-uniformity of the electric field, as the length of the charging channel L is shorter than its' width at the smallest value of L. Therefore, the maximum in the charging efficiency occurs there where the $n_{ion}t$ -product is sufficiently high for obtaining a high intrinsic charging efficiency, but where L is not too high in order to minimize the losses of charged particles. A higher value of the gas flow rate ϕ leads to a lower $n_{ion}t$ -product at constant L (Fig. 6.1.3), so that a longer charging channel is necessary.

The present charger does not use a sheath gas flow along the walls or wire meshes. A sheath flow have been used in order to decrease the losses of charged particles. Chen and Pui (1999) report reaching an extrinsic charging efficiency of 65 % (with a definition based on absolute particle number, not on particle concentration) for particles with a diameter of 10 nm. However, a large sheath gas flow is applied which results in a dilution of the aerosol by a factor of four. This dilution is usually not desired. Using our definition of extrinsic charging efficiency (eq. 6.2.1), an extrinsic charging efficiency of 16 % would result.

6.2 A Differential Mobility Analyzer design for low pressures

The differential mobility analyzer (DMA) is the predominant instrument for measuring the size distribution of submicron aerosols. Additionally, the instrument is more and more being used as a source for delivering particles with a narrow size distribution. In a DMA, charged particles are separated according to their electrical mobility. In a cylindrical DMA, the median value of the electrical mobility of the classified particles is given by (Knutson and Whitby, 1975):

$$Z_p = Q_c \frac{\ln(R_2 / R_1)}{2\pi L V} \qquad (6.2.1)$$

in which L is the effective electrode length, R_1 and R_2 the inner and outer radii, V the applied voltage and Q_c the flow rate of the sheath gas. In another DMA design, the radial DMA originating from Pourprix and tested by Fissan *et al.* (1998) the electrical mobility is given by:

$$Z_p = \frac{Q_c h}{\pi\left(R_2^2 - R_1^2\right)V} \tag{6.2.2}$$

in which h is the distance between the electrodes. Both DMA types are available in several design types, and their performance was tested by Fissan *et al.* (1996). In Fig. 6.2.1 both types are shown.

The mobility Z_p can be related to a mobility-equivalent diameter:

$$Z_p = \frac{neC_c}{3\pi\mu d_p} \tag{6.2.3}$$

where n, e, C_c, μ and d_p are the number of elementary charges, the elementary electrical charge, the Cunningham correction factor, and the gas viscosity, respectively. For charged nanoparticles, the number of elementary charges is usually one.

The performance and suitability of a DMA for a certain application, i.e a given flow rate and pressure, is a function of the following instrument characteristics:

- Deviation from the ideal transfer function, e.g. by diffusional broadening effects. Diffusional broadening is caused by the Brownian movement of the nanoparticles between inlet and outlet slits, and increases with decreasing particle size.
- Particle losses inside the instrument, e.g. by diffusional or electrostatic losses.
- The maximal voltage before sparking between the two electrodes occurs.
- The maximal flows allowed in the instrument before turbulence occurs.
- Pressure drop inside the instrument.

The dynamic range of the instrument is usually limited to smaller particle sizes by the allowed value of the diffusional broadening , and to larger sizes the limitation is given by the voltage at which sparking occurs.

DMA's are designed to operate at atmospheric pressure. However, many nanoparticle synthesis systems operate in the mbar-range. There has been only one report on a DMA capable to operate under lower pressure conditions, 70-760 Torr (Seto *et al.,* 1997). The instrument is of the cylindrical type.

There are several considerations for low-pressure operation. When decreasing the pressure, the diffusion coefficient of particles increases as it is a linear function of the mean free path. This can be offset by increasing the velocity inside the instrument. Seto *et al.* (1997) found out that the performance could be kept on an acceptable level

when keeping the mass flow rate of the gas constant. A constant mass flow rate implies a higher gas velocity, as the product of velocity and density is constant.

In this work, a radial DMA is taken as geometry. The main reason is that the instrument is easily constructed in comparison to cylindrical DMA's. This can clearly be seen in Fig. 6.2.1. The performance of radial DMA's at atmospheric pressure has been experimentally found to be equal or even surpass that of a cylindrical geometry.

The tendency of a flow to become turbulent is determined by the Reynolds number. For a simple tube flow, it is given by:

$$\mathrm{Re} = \frac{\rho v D_{tube}}{\mu} \tag{6.2.4}$$

with ρ as gas density, v as gas velocity and D_{tube} as tube diameter. When decreasing the pressure by a factor C, the gas velocity v is not affected. The gas density changes with a factor $1/C$ and the gas velocity is multiplied with a factor C. This means that the Reynolds number is not affected by changing the pressure. For geometries other than a tube, the hydraulic diameter D_h has to be used in eq. 6.2.4. The conclusion that the Reynolds number is independent of system pressure is also valid for other DMA geometries, as the pressure does not change the hydraulic diameter. For the cylindrical DMA geometry, the hydraulic diameter can be derived to be:

$$D_h = \frac{2\left(r_2^2 - r_1^2\right)}{r_1 + r_2} \tag{6.2.5}$$

For a radial DMA, the hydraulic diameter is:

$$D_h = 2h \tag{6.2.6}$$

The standard conditions for DMA operation are an aerosol flow of 1.45 slm, sheath flow of 15 slm and N_2 carrier gas at STP. It can be shown that most cylindrical DMA's operate with Reynolds numbers below 1000. However, for the radial DMA the velocity is highest close to the central exit. When calculating for r=1.5 mm the Reynolds number, a value of 3890 is found which is in the turbulent range. Interestingly, the existing instrument does not show signs of turbulence which would have been detected by an increase in the transfer function. This can be understood by the practical experience that it takes some time for turbulences to develop. Because the flow is initially laminar and the actual position where the flow becomes turbulent is close to the exit, it looks like turbulence did not develop. The system is, however, sensitive to small disturbances.

a)

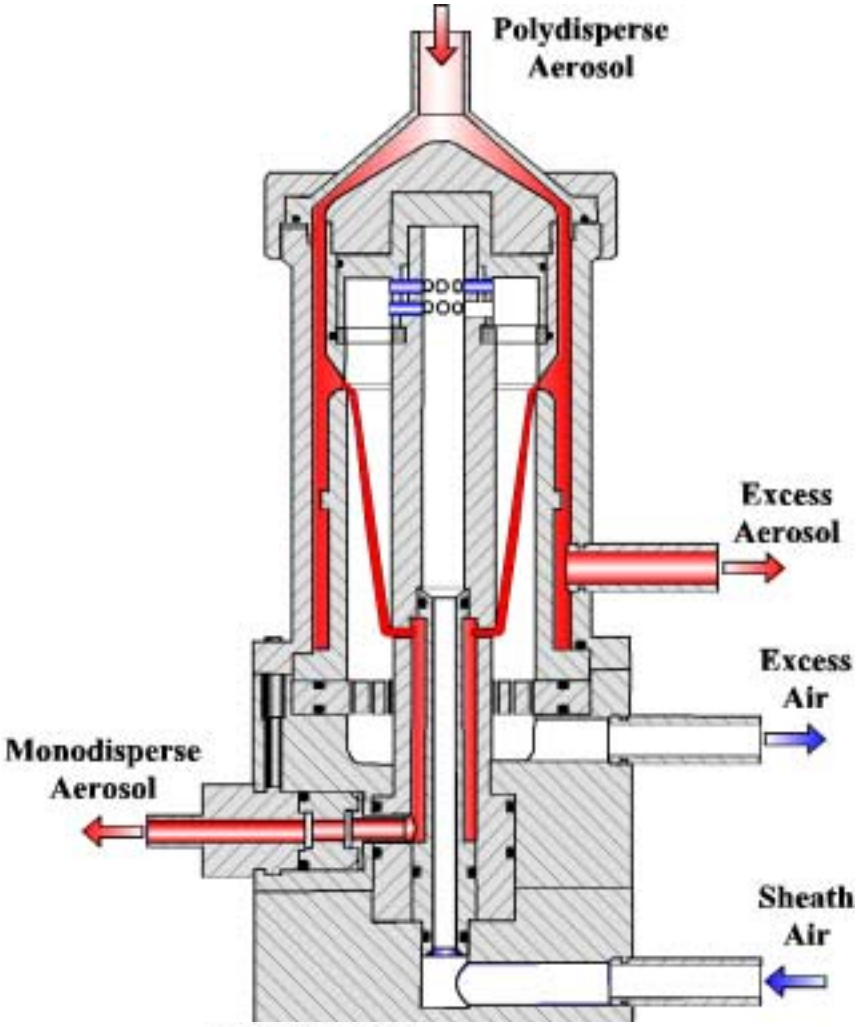

b)

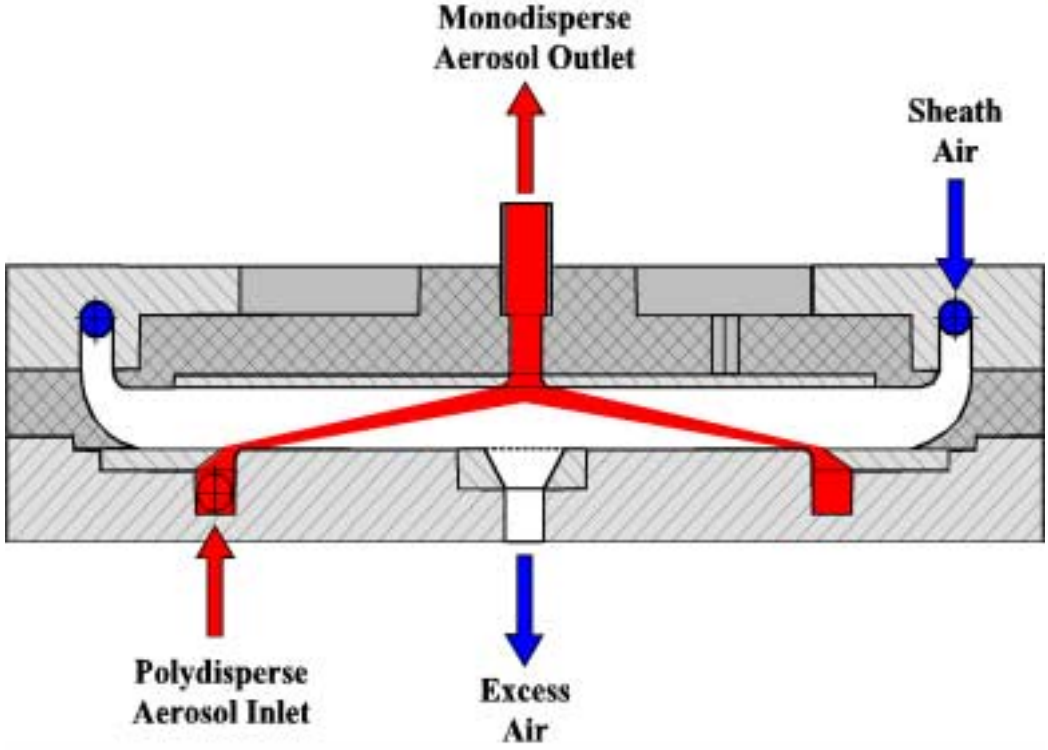

Fig. 6.2.1. a) Cylindrical (Chen et al., 1998) and (b) radial (Fissan et al., 1998) DMA design.

We can now derive the ratio of the Reynolds numbers of the two geometries:

$$\frac{\mathrm{Re}_{rad}}{\mathrm{Re}_{cyl}} = \frac{A_{cyl} D_{h,rad}}{A_{rad} D_{h,cyl}} = \frac{r_{1,cyl} + r_{2,cyl}}{2 r_{rad}} \tag{6.2.7}$$

Because the typical radial dimensions of a cylindrical DMA are in the cm-range and in the mm-range for a radial DMA, the radial DMA with a central outlet shows a higher tendency for turbulence. One solution to decrease the Reynolds number for the radial DMA which is adopted here, is not to use a central outlet but a slit at some distance to the central axis. This increases the value of r_{rad} and decreases thus the value of the Reynolds number.

When designing a DMA, an important performance criterion is the diffusional broadening at the lowest particle diameter to be classified. This broadening might be estimated by means of the Péclet number, which is the ratio of the particle convective to diffusive transport. For the radial DMA, the Péclet number is given by:

$$Pe_{rad} = \frac{h Q_c}{\pi \left(R_2^2 - R_1^2 \right) D} \tag{6.2.8}$$

in which D is the particle diffusion coefficient. Fissan *et al.* (1997) showed that the half-width of the transfer function increases with decreasing Péclet number, based on the mean velocity. This can be seen in Fig 6.2.2. This diagram shows that the difference from the ideal value of 0.1 becomes more than 50 % when the Péclet number becomes below smaller than 1000. This result can be used in order to estimate for given geometry and experimental conditions the smallest particle diameter which can be fractionated with reasonable accuracy.

Practical experience showed that a DMA configuration usually allows a particle size range between one and two decades. Therefore it was decided to design two DMA's, so that by combining the two instruments a larger measurement range is obtained. In table 6.2.1. the chosen geometry parameters are shown. Two slits, a larger one for the aerosol entrance and a smaller one for the monodisperse aerosol outlet are used. The Reynolds number at the aerosol outlet is now in the laminar range. For the calculations which assume a slit with zero width, the middle of the slit is used as the radial position of the slit.

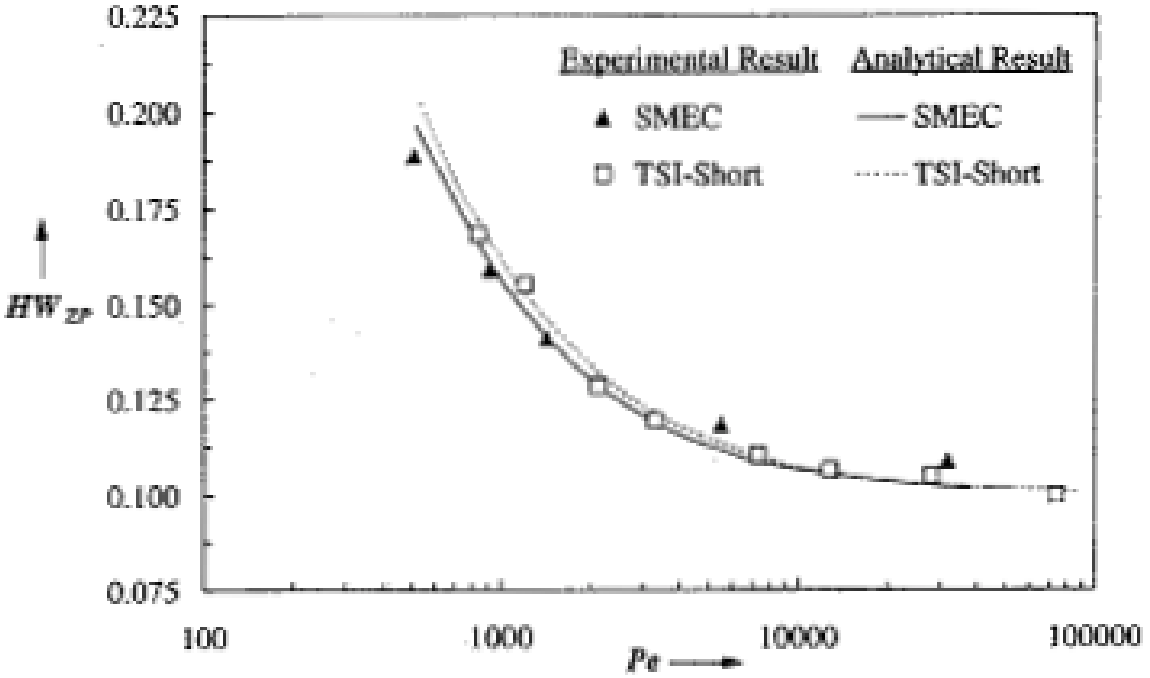

Fig 6.2.2. Experimental and analytical half-width HW of a radial DMA (SMEC) and a cylindrical DMA (TSI-short) as a function of the Péclet number. The sheath flow rate is 10 slm and 15 slm, respectively (Fissan et al., 1997).

Table 6.2.1. Geometry parameters (in mm) of the proposed low-pressure radial DMA's.

type	$R_{1,\ inner}$	$R_{1,\ outer}$	$R_{2,\ inner}$	$R_{2,\ inner}$	h
LP-RDMA1	4.6086	6.6517	21	21.9876	10
LP-RDMA2	4.6086	6.6517	82	82.9876	15

For predicting the measurement range of the instruments at a lower pressure, the following procedure is followed. For each particle size, the Péclet number is calculated for the usual operation at 1 bar and also at 100 mbar. This is shown in Fig. 6.2.3 for both DMA geometries. The smaller one (LP-RDMA1) is usually operated with higher flow rates (15 slm) in order to reduce the diffusional losses, whereas the larger one (LP-RDMA2) is operated with a lower flow rate in order to enable size fractionation of larger particles.

a)

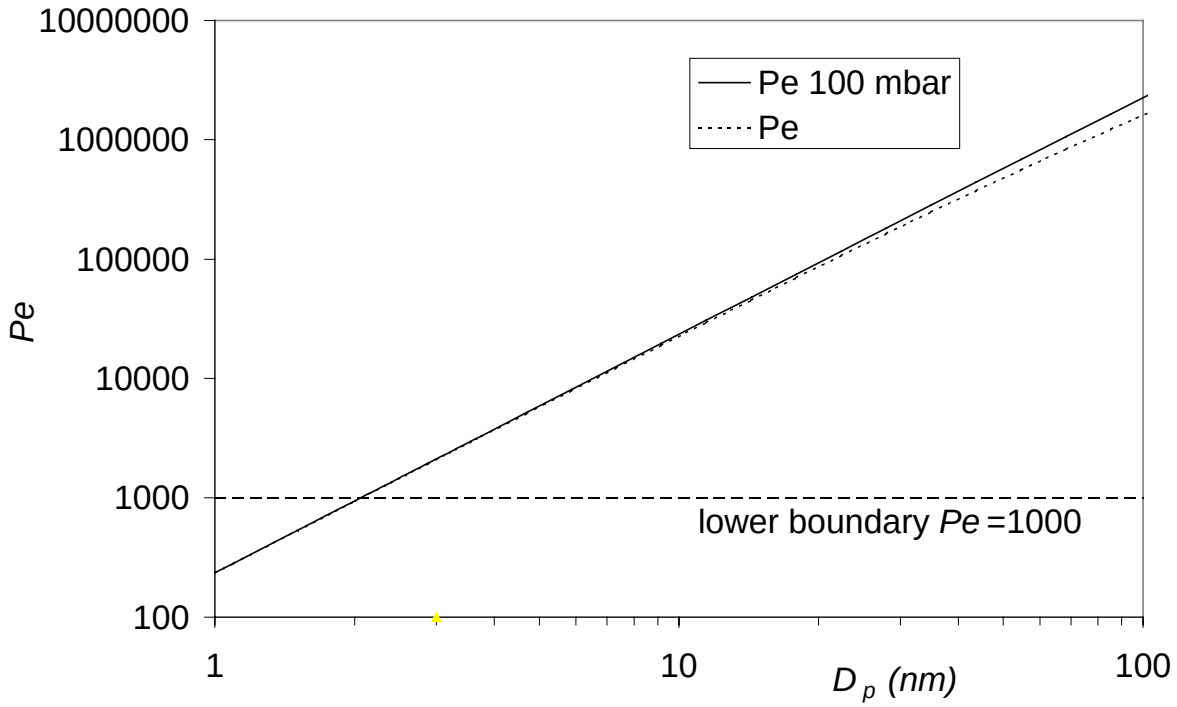

b)

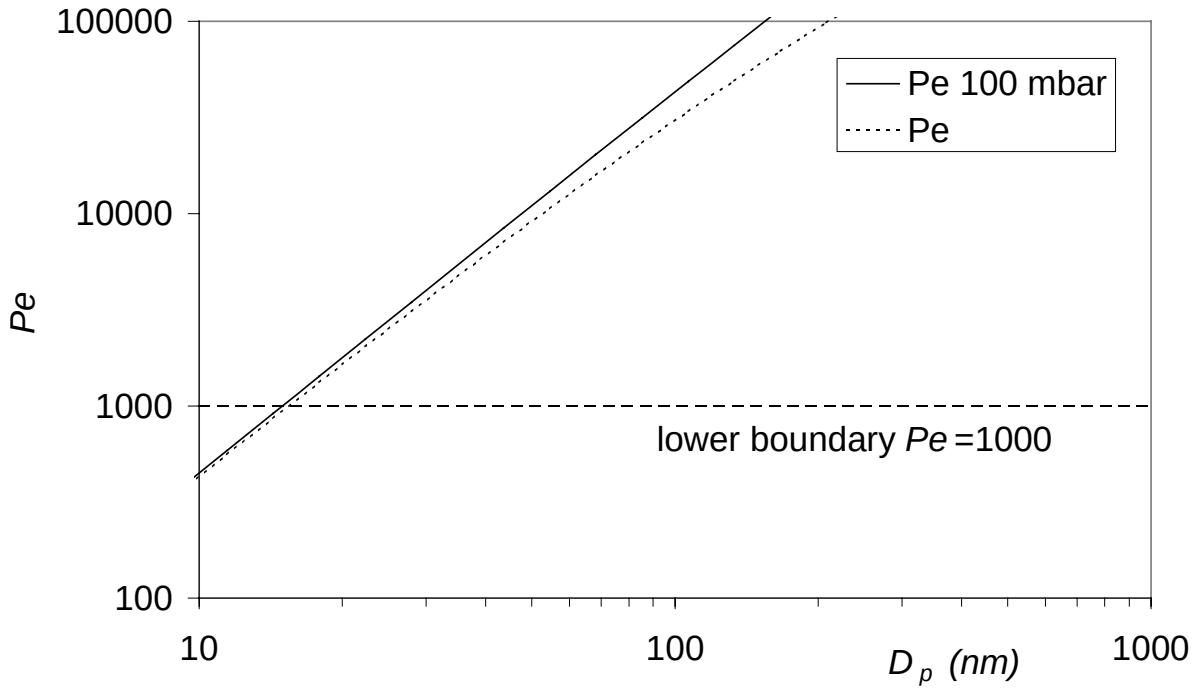

Fig. 6.2.3. Péclet numbers as function of particle diameter for a) LP-RDMA1 with 15 slm sheath gas and for b) LP-RDMA2 with 3 slm sheath gas.

It is interesting to see that the Péclet number is not changing substantially when operating at lower pressures as compared to standard conditions. This is due to the mass flow rate being constant, so that the actual velocity increases. The increased diffusion coefficient of particles at lower pressures is compensated by the higher flow rate at lower pressures. Because the ratio of volumetric flow rate and diffusion coefficient is used in the Péclet number, it does not change. For larger particles the deviation is due to the fact that the particles are not any more in the free-molecular regime for which the diffusion coefficient is inversely proportional to pressure. From the figures it becomes clear that, when taking Pe=1000 as lower limit where adequate fractionation is still possible, the LP-RDMA1 has a lower particle diameter limit of 2 nm and the LP-RDMA2 of about 15 nm.

The upper limit for the particle size is determined by the voltage which can be applied before sparking occurs. The maximal field strength is, however, a pressure-dependent function and decreases when the pressure decreases, until some point in the sub-mbar range where it increases again which is not of interest here. In Fig. 6.2.4 the voltage which has to be applied is shown as function of particle diameter. As indicated in the figure, the maximum voltage which can be applied is lower in case of the lower pressure. The upper particle limit with the given sheath flow rates is 30 nm for the small type and 250 nm for the large type. These are of course estimations and will have to be experimentally determined.

The preceding engineering estimations result in a particle size range of 2-30 nm and 15-250 nm at 100 mbar for the small and large type, respectively. It can be concluded that the lower particle limit is not affected essentially by pressure decrease but that the reduced maximal field strength results in a lower maximum particle size than in case of standard conditions. Each particle size decade probably requires an appropriate DMA.

After these quantitative estimations of the operation range of the two proposed radial DMA's, construction designs were made. The design is shown schematically in Fig. 6.2.5. Important features are:

- The aerosol outlet is a slit.
- The excess gas flow is directed toward the outlet by means of a protrusion in the middle of the central electrode.
- The electric field is almost perfectly homogeneous inside the fractionation channel.
- Stainless steel is used for all metal parts and delrin is used as isolation material.
- There are no holes for screws at the outside of the instrument, as this is not compliant with the requirement for vacuum tightness. Much care was taken to put the screws inside the vacuum chamber, but outside the main fractionation channel. The design requires the upper and lower parts to be assembled before final assemblage.

a)

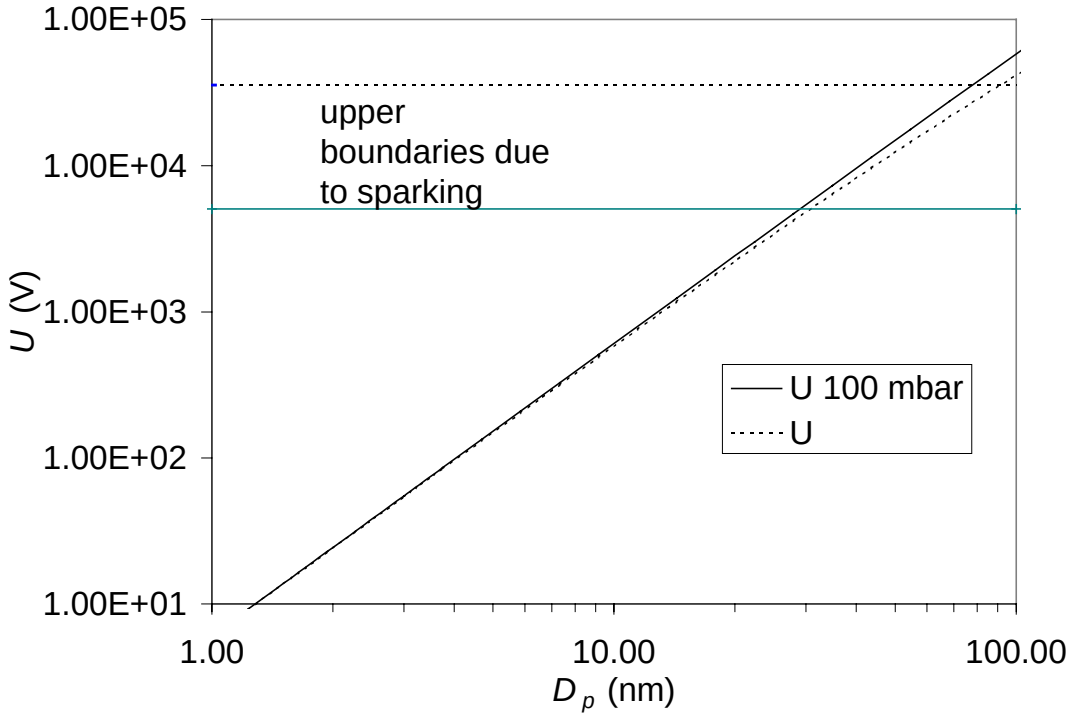

b)

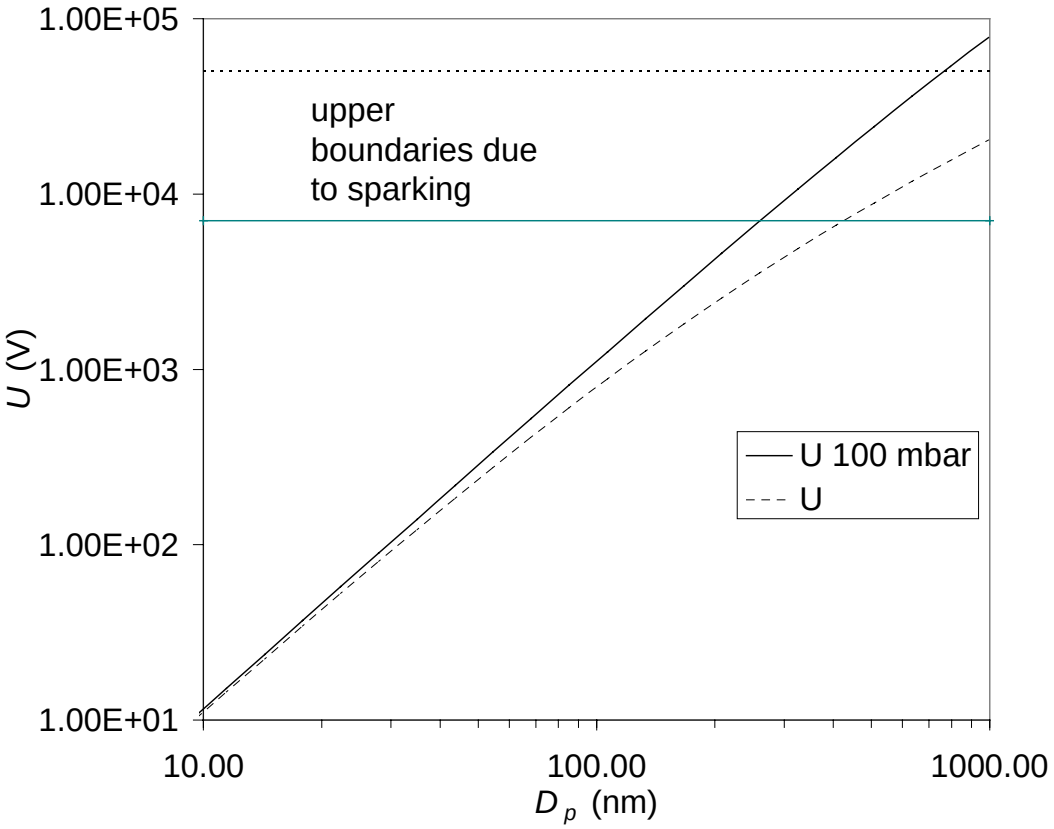

Fig. 6.2.4. Voltage to be applied as function of particle diameter for a) LP-RDMA1 with 15 slm sheath gas and for b) LP-RDMA2 with 3 slm sheath gas.

- Standard KF16 vacuum connections are used as gas and aerosol in- and outlets.
- The sheath gas is introduced through four large inlet ports. A porous inset (not shown in the figure) will be used as flow laminarisator. The excess gas outlet has only one outlet port.
- The DMA can very quickly be opened and cleaned, which is important for materials synthesis applications.
- Both aerosol in- and outlet are positioned at the axis of the instrument.
- The aerosol inlet does not have a swirling velocity compound in tangential direction
- The design is such that the main components can easily be replaced. Several other delrin isolation inserts allow the distance between the electrodes to be easily modified.
- The internal tightness of the different flow channels is obtained by means of O-rings.

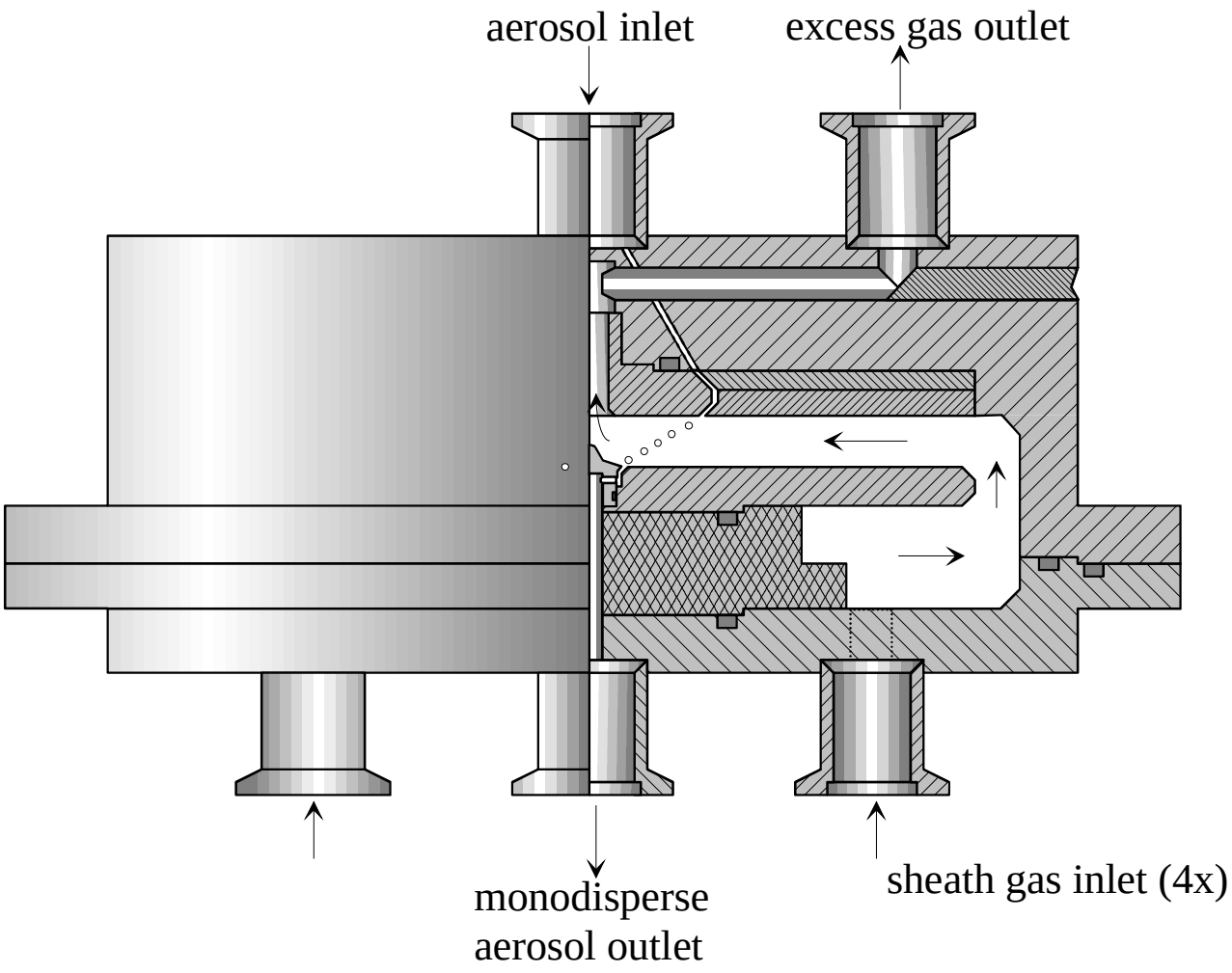

Fig. 6.2.5. Schematic design of the new LP-RDMA.

The main uncertainties concern the pressure drop in the instrument and the distribution of the aerosol flow inside the inlet slit. These will have to be resolved experimentally.

6.3 An electrostatic precipitator for measurements under clean conditions

A nanoparticle aerosol will be of no practical use when the particles are not in some way deposited on a substrate or imbedded in some matrix. In the method applied in this work to produce well-defined nanoparticles, the particles leaving the process are unipolarly charged. A simple method to deposit them onto a substrate is to use an electrostatic precipitator (ESP). Here, a central electrode connected to a high voltage (5-15 kV) with the opposite polarity as that of the particles extracts the nanoparticles from the flow. When a substrate is placed on the central electrode, a thin layer of nanoparticles develops in form of a circular deposit with a diameter of 5-10 mm, depending on particle size, electrode diameter and voltage. The ESP is schematically shown in Fig. 6.3.1.

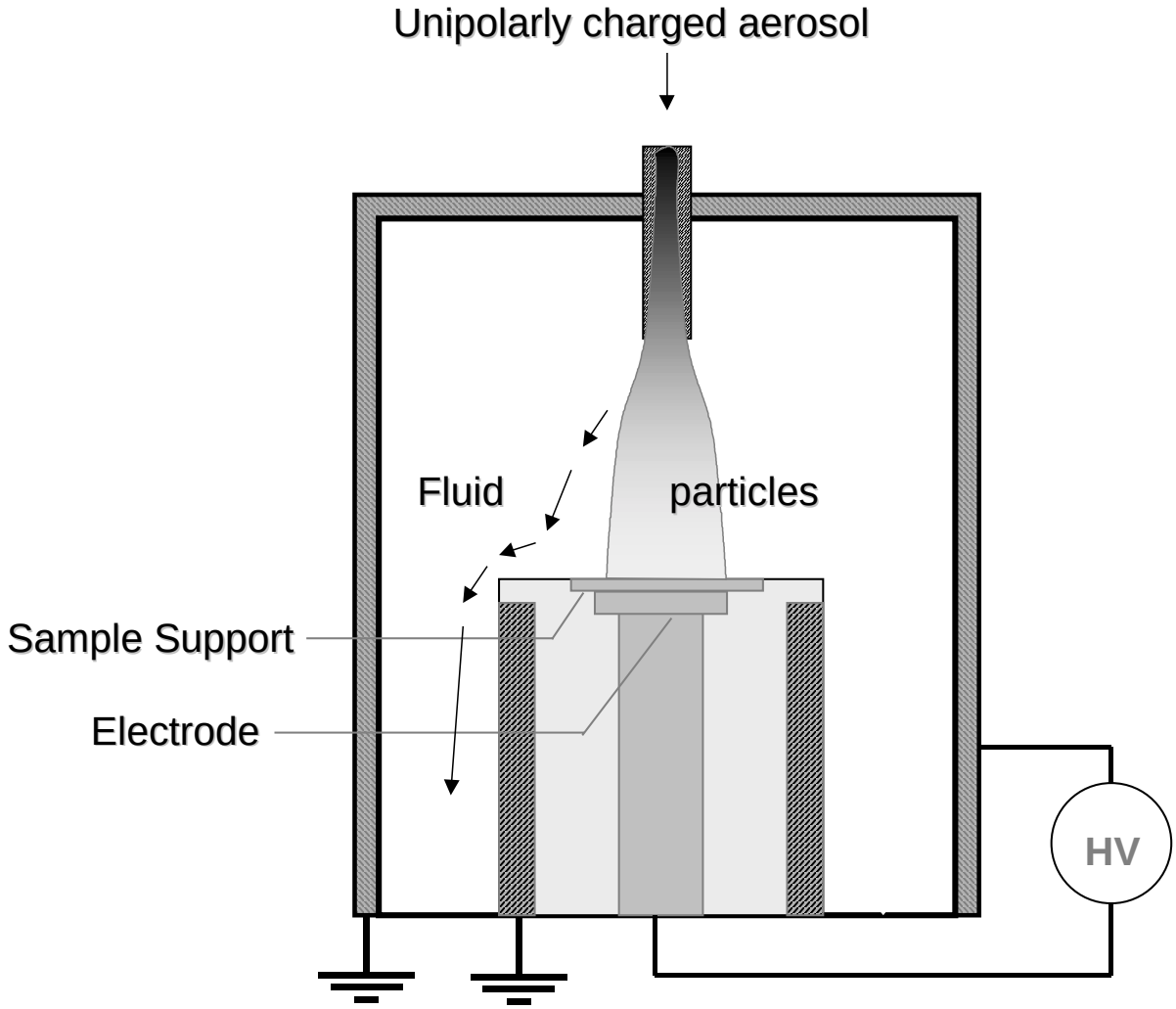

Fig. 6.3.1. Schematic view of the electrostatic precipitator (ESP).

The first version of the ESP was developed by Dixkens and Fissan (1997) and was subsequently adopted for our goals. The modifications include construction from stainless steel, an easily exchangable central electrode with the goal to change its diameter and the possibility to insert a small inlet tube which extends closer to the electrode. Over a critical orifice in the central inlet the apparatus can be used as a low-pressure impactor when a pump is connected to the gas outlet. This second mechanism for particle deposition onto a substrate allows the deposition of uncharged particles and increases the deposition velocity so that particle adhesion can be improved. Furthermore, it is expected that films formed by uncharged particles are more homogeneous than those formed by charged particles, as charged particles can lead to the formation of dendrites, long particle chains pointing away from the surface. The present version allows to apply both deposition mechanisms and even a combination of them.

During preliminary measurements of electrical properties of thin films of PbS nanoparticles, it was found that measurements in ambient air were not particularly reproducable. The substrates with deposited nanoparticles had to be taken from the ESP toward a probe station, so that surface contamination occurred. An measurement of the electrical properties without air exposure is preferable and thus a special ESP has been constructed. It consists of a deposition chamber, where the ESP itself is situated, and a chamber which can be evacuated in which the deposition electrode can be placed after particle deposition. The electrical contact is obtained over micromanipulators with meaurement tips. The substrate is in its measurement position placed close to an observation window for accurate observation of the contacting process by means of a macroscope. Fig. 6.3.2 shows the schematics of the M-ESP.

The advantage of the system is that immediately after particle deposition, the electrode can be brought in measurement position and evacuated. A pressure of 10^{-3} mbar was obtained, which was limited by the characteristics of the pump. The instrument is constructed such that the substrate can easily be connected to a liquid N_2-cooling system.

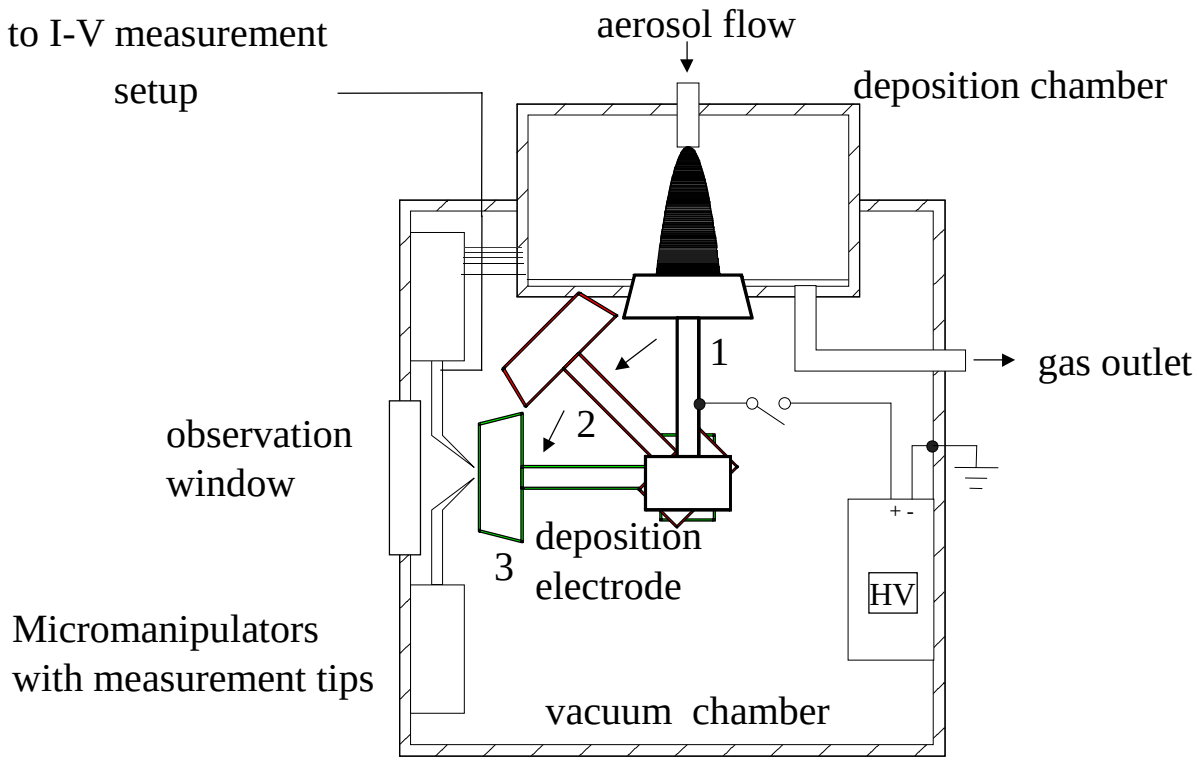

Fig. 6.3.2. Schematics of the measurement-ESP (M-ESP).

6.4 Conclusions: Instrumentation for controlling nanoparticle behavior

In this Chapter, newly developed instrumentation for controlling nanoparticle behavior 'in-flight' is described which allow to obtain more control over processes which are essential for the synthesis and handling methods chosen in this work. These processes are nanoparticle charging, nanoparticle size fractionation and nanoparticle deposition.

A newly developed nanoparticle charger, the twin-Hewitt charger, allows a larger fraction of the nanoparticles to be charged, which is important to get a higher yield. A higher yield would result in a shorter deposition time, which is important because the deposition of thin nanoparticle layers takes at present still too long. The instrument has been extensively investigated experimentally in order to find the optimal charging conditions.

Differential Mobility Analysis at lower pressures than atmospheric pressure has been investigated theoretically. It was found that the lower particle limit is not changed fundamentally with lower pressures when keeping the mass flow rate constant, but that the higher particle limit is decreased due to decrease of the maximum allowed field strength. A Differential Mobility Analyzer design for low pressure has been presented. It is important to perform size fractionation at pressures lower than atmopsheric

pressure, as usually the system pressure is decreased in order to get a higher yield of smaller nanoparticles.

An Electrostatic Precipitator has been developed which allows the investigation of electrical properties of nanoparticle films under clean conditions direct after deposition. This is especially important for semiconductor nanoparticles, where the surface influences the optical and electronic properties.